



Enhancing the Robustness of Hybrid Metal-Composite Connections Through 3D Printed Micro Penetrative Anchors

Luca Raimondi^{1,2} · Luca Tomesani^{1,2} · Andrea Zucchelli^{1,2}

Received: 17 January 2024 / Accepted: 18 March 2024
© The Author(s) 2024

Abstract

This work proposes a novel solution for manufacturing hybrid metal-composite joints, in which different pin shapes are evaluated for their capability to penetrate long carbon fiber epoxy composites successfully and for the mechanical behavior determined by each configuration. On the metal side, pins are manufactured by Laser Powder Bed Fusion (LPBF), downsizing the currently adopted solutions and, at the same time, developing new blocking features aimed at enhancing the mechanical properties of the joint. The different configurations were evaluated in two distinct experiments: the first to evaluate the induced defects in the composite substrate and the second to characterize the mechanical behavior of the joint. It emerges that smaller pins produce much less damage and misalignments in the composite structure with respect to the conventional pin solution, whereas the new “blocking features” configurations consistently increase maximum pullout load and energy with respect to the conventional pin solution, with the same level of fiber damage.

Keywords Hybrid metal-composite Joints · Micro-pins · Joints/joining · Failure

1 Introduction

In recent years, there has been a notable trend in the aerospace, automotive, and robotics industries towards developing lightweight, structurally efficient composite structures by incorporating dissimilar materials, such as metals and polymeric composites [1, 2]. This strategic combination of materials with disparate physical and mechanical properties allows for the precise tailoring of component characteristics, enabling designers to select the most appropriate materials for specific, localized requirements. Composite materials are highly prized for their superior strength-to-weight ratio, customizability, corrosion resistance, and design flexibility, making them ideal for lightweight, high-performance applications. How-

✉ Luca Raimondi
luca.raimondi@unibo.it

¹ DIN – Università di Bologna, Viale Risorgimento 2, Bologna 40136, Italia

² CIRI-MAM – Università di Bologna, Viale Risorgimento 2, Bologna 40136, Italia

ever, composite materials also present challenges, including limited damage tolerance and difficulty in joining and repairing [3–5]. Similarly, metallic materials are highly valued for their inherent strength, ductility, machinability, resistance to high temperatures, wear resistance, and ease of joining, which make them suitable for a broad range of applications despite their relatively high density and potential for corrosion. Optimizing the interfaces between the different materials represents the most remarkable technological challenge to fully exploit the potential of multi-material hybrid structures. This optimization must address a variety of tasks arising from the different mechanical, physical, and chemical properties, such as varying stiffness, thermal expansion, and chemical compatibility [6]. Bolting, bonding, welding, self-piercing riveting [7] have been traditionally applied to join these dissimilar materials [8]. A promising technology with the potential to create multi-material components consisting of a metal part and an endless fiber-reinforced polymer part is the use of 3D metallic pins structure protruding from the bulk metal substrate and embedded into the composite substrate to facilitate load transfer and substantially influencing the resulting structure's strength, stiffness, and damage tolerance [9, 10]. Pin manufacturing techniques include the Surf-i-Sculpt™ laser treatment to produce COMELD™ pins [11], cold metal transfer (CMT) [12], laser cutting and cold metal forming to form pins out of a metal sheet [13, 14], and laser-based powder bed fusion (LPBF) additive manufacturing (AM) [15–17]. In the current state of the art, LPBF has emerged as the most versatile solution for manufacturing thin, high-performance metallic pin structures directly on existing metal substrates of various materials [18, 19]. This manufacturing process offers an unrivaled ability to tailor the design of pin geometry when compared to Surf-i-Sculpt™, CMT, or metal forming, maintaining the potential to reduce AM build time and cost and allowing the retrofitting of existing components by adding 3D metallic pins on their surface [20]. During the LPBF manufacturing of thin structures, the laser melting of metal powders can result in surface irregularities and roughness, as noted in [21]. Additionally, the rapid solidification of molten metal can lead to partially fused particles and surface defects, as described in [22]. Numerous authors have shown that these imperfections deliver added value in multi-material joining by establishing supplementary interlocking mechanisms between the metal and composite interfaces, significantly enhancing the joint's load-bearing capacity [15, 23, 24]. The insertion of additively manufactured 3D pins into a composite substrate can lead to defects such as in-plane fiber crimping and the formation of resin-rich regions [20, 25], similar to those encountered in z-pinning, which is an established technique in the field of composite materials [26, 27]; these defects are localized in a limited region surrounding the pin, impacting the original fiber-polymer distribution and locally affect the mechanical properties of the substrate [28, 29]. Reducing the diameter of the z-pin in the range of 0.3 mm ÷ 0.5 mm has been proven to provide a strategic pathway to mitigate those defects, as suggested by several recent researches [30–32]. To date, proposed LPBF AM 3D pins are mainly cylindrical [15, 16, 28, 33], with a diameter in the range of 1.00 mm ÷ 1.5 mm [15–17, 28, 33, 20]. This implies that there might be an opportunity for improvement by reducing diameters, as observed in the successful mitigation of defects through smaller z-pin diameters in the micrometric range. Furthermore, significant optimization opportunities of the interface are given by fine-tuning the pin diameter; in fact, the interfacial strength between the pin and the composite linearly increases with pin diameter [34] and, at the same time, the material consumption is a quadratic function of pin diameter. In this work, the transition to smaller diameters of the additively manufactured 3D pins in hybrid multi-material joints is

experimentally evaluated to understand the effect of geometrical parameters variation on the main processing issues. Several metal-composite hybrid joints with different pin geometries were produced, in which the effect of pin diameter and pin shape were investigated to catch the opportunities given by the precise forming capability of LPBF technology. The different configurations were then used for two distinct experiments: the first aimed at evaluating the induced defects in the composite substrate and the second for the mechanical characterization of multi-material components.

2 Materials and Methods

This section is conceptually split in five. The materials and methods used to produce metallic and composite substrates are described in Sect. 2.1 and Sect. 2.2, respectively; Sect. 2.3 describes the methodology used for fiber misalignment evaluation. The methodology for mechanical characterization of multi-material parts and data elaboration are reported in Sect. 2.4. Section 2.5 illustrates the methodology used for the morphological characterization of the fractured surface of the multimaterial joint.

2.1 Metal Substrates

The metallic substrates were created using 12.2Cr-10Ni-1Mo-1Ti-0.6Al Precipitation-Hardening Stainless Steel (PH-SS) via the LPBF process. This material was selected for its ultra-high strength, satisfactory ductility, and excellent anti-corrosion properties [35]. A SISMA MYSINT100 (SISMA SpA, Italy) machine was used to grow penetrative reinforcements directly on 99 mm diameter cylindrical building platforms. Gas atomized Böhler M789 powder, with particles ranging in size from 15 [μm] to 45 [μm], obtained from Böhler Edelstahl (Kapfenberg, Austria) was used for sample production. The printing parameters were chosen to achieve higher component density [36]: 250 W laser power, 50 μm spot diameter, and 20 μm layer thickness. To ensure product quality, prevent oxidation, and control porosity, a stable flow of inert nitrogen gas was introduced into the chamber before printing, keeping the oxygen content below a 0.2% threshold. Four different 3D pin geometrical configurations were considered for the manufacturing of multi-material components: a conventional cylindrical pin (Fig. 1a), a thin cylindrical pin (Fig. 1b), an arrow shape cylindrical thin pin (Fig. 1c), and a Two-Headed Arrow shape cylindrical thin pin with multiple features (Fig. 1d). All selected geometries present a 90° conical tip to ease insertion [37] and a small fillet of 0.13 mm radius to prevent a potential reduction in diameter at the pin root during printing [38]. Two different platforms, namely Platform A and Platform B, were manufactured. Platform A, enclosing seven sectors with five different pin shapes, was designed to allow defect evaluation in the infiltration experiment; Platform B, enclosing 12 single-pin adherends, was designed to fabricate samples for mechanical characterization.

Platform A (Fig. 2a) has seven 20 mm x 20 mm distinct sectors composed as following:

- One unpinned sector used as a reference.
- 16 conventional cylindrical pins (F 1 mm) distributed in a square pattern.
- 32 thin cylindrical pins (F 0,5 mm) disposed in a chequer pattern.
- 36 thin cylindrical pins (F 0,5 mm) disposed in a square pattern,

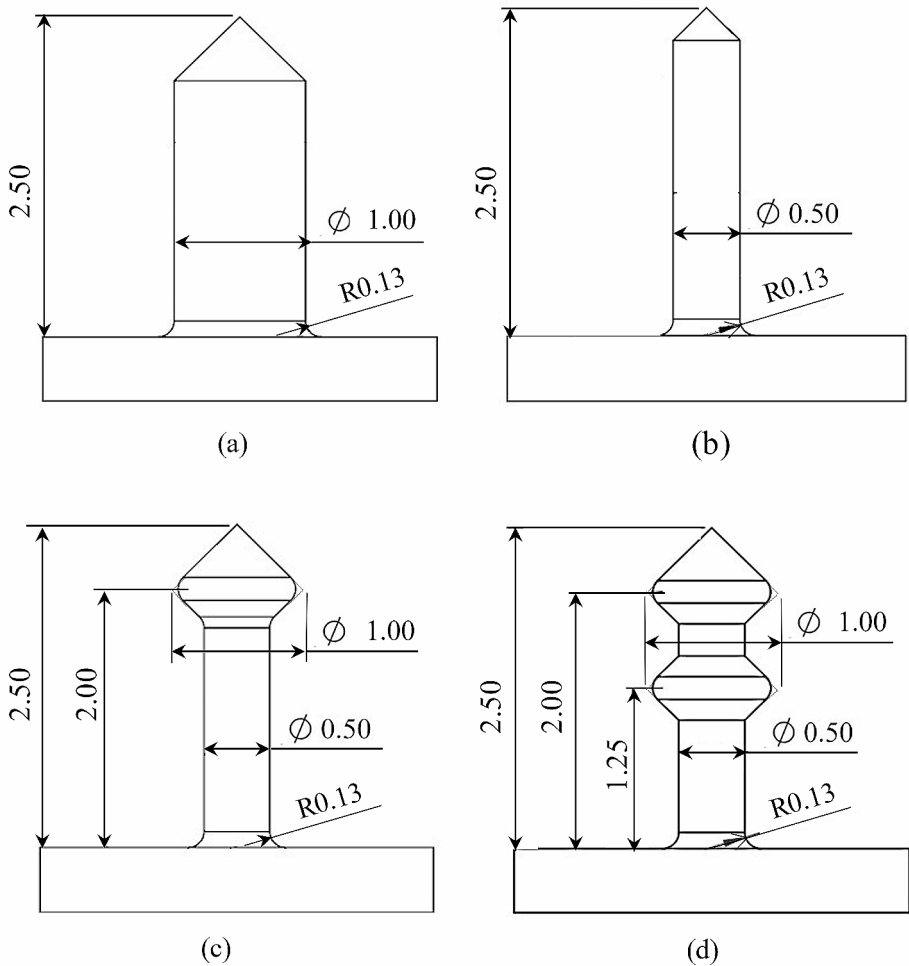


Fig. 1 Pin geometries. (a) conventional large cylindrical, (b) thin cylindrical, (c) arrow, and (d) two-headed arrow

- 36 single-arrow cylindrical pins disposed in a square pattern.
- 36 two-headed Arrow cylindrical pins disposed in a square pattern.
- 36 reverse cone cylindrical pins disposed in a square pattern.

A reverse cone cylindrical pin was introduced as a reference point, to measure the exact positioning in thickness while polishing according to the protocol described in Sect. 2.3. Care was taken to optimize the pin distribution to prevent the formation of resin channels or scatters in waviness on the composite substrate during insertion [26]. An equally spaced pattern of four times the diameter of the pin was adopted as a compromise between high density and potential defect mitigation.

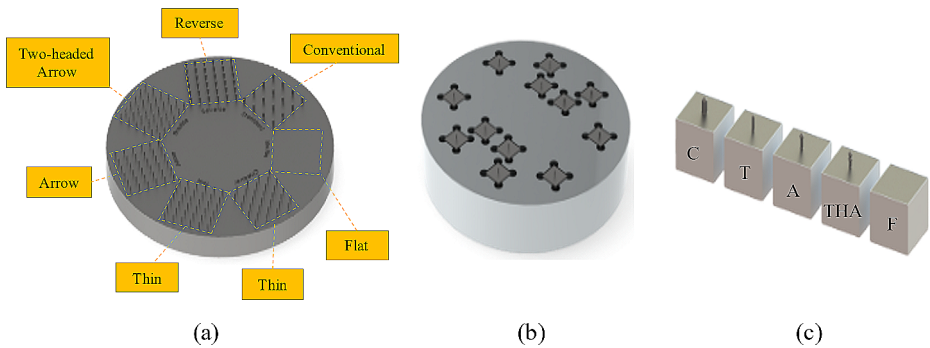


Fig. 2 AM Pins on platforms. (a) platform A with seven sectors and five pins design for defect evaluation (b) platform B for single pin specimens sample holding for mechanical characterization (c) single pin adherends for mechanical characterization

Platform B (Fig. 2b) enclosed 12 separate cubic elements for mechanical testing sample fabrication; on each cube, one pin was printed; in a later stage, after the composite insertion process on the whole platform, the metal elements were simultaneously extracted altogether with the composite; finally, the samples were cut one from the other by low-speed sawing, to avoid sample damage. On platform B the printed elements were the following: (i) 3 elements with one conventional cylindrical pin each (sample C, Fig. 2c) (ii) 3 elements with one thin cylindrical pin each (sample T, Fig. 2c) (iii) 3 elements with one Arrow pin each (sample A, Fig. 2c) (iv) 3 elements with one two-headed arrow pin each (sample THA, Fig. 2c) and (v) 3 reference flat samples for comparison (sample F, Fig. 2c). The samples produced were then subjected to mechanical testing as reported in Sect. 2.4.

2.2 Composite Substrate Preparation and Insertion

A commercial unidirectional prepreg supplied by Delta-Tech S.p.A. (IT) was used to create the composite substrate. The prepreg is composed of high strength/standard modulus Toray T700S carbon fibers impregnated with 40% (V_f) high toughness and slow-curing DT120 resin. The areal weight of the tape is 150 g/m² (approximate, as supplied), and its nominal thickness is 0.3 mm ± 0.4%. This prepreg's initial misalignment angle was measured to be 0.91°, following the procedure reported in [39]. The prepreg roll was extracted from cold storage and put in a white chamber for 3 h. Square plies of 10 mm x 10 mm were cut to produce the composite substrate for mechanical testing, while square plies of 20 mm x 20 mm were extracted to produce the composite substrate for misalignment analysis. The joints were constructed by initially arranging the plies into sub-laminates of five compacted layers in a $[0]_5$ configuration. Each sub-laminate was manually pressed onto the pins until the composite and metal substrates interacted. Both prepreg and metal substrate were pre-heated at approximately 40 °C to facilitate insertion. This procedure was iterated until the composite substrate's thickness matched the total length of the pin. Afterward, an extra $[0]_5$ sub-laminate was added to avoid pin piercing through the composite substrate. To mitigate the worsening of fiber waviness, multi-material samples were cured using the vacuum bagging technique. Samples were placed in an environmental chamber and subjected to a ramp of approximately 1.5 °C/min followed by 4 h hold at 130 °C. A constant vacuum of approxi-

mately 101 kPa was applied and maintained throughout the curing cycle to eliminate voids, air bubbles, and excess resin from the laminate.

2.3 Fiber Misalignment Evaluation

Optical microscopy was used to investigate the in-plane fiber misalignment produced on the composite substrate by the insertion of the different pin shapes. The specimen underwent a multi-step preparation process. Initially, it was conditioned through wet grinding using abrasive papers of varying grit sizes, including 240, 400, 800, 1000, and 2500. Subsequently, a two-step polishing procedure was carried out using a water-based alumina suspension. In the first step, alumina particles ranging from 3 μm to 1 μm were applied on a low-napped silk polishing pad. In the second step, a high-napped silk polishing pad was used with alumina suspension containing particles ranging from 0.5 μm to 0.3 μm . Care was taken in optimizing force, platen speed, and polishing time to avoid pullouts and artifacts. After each polishing step, the samples were cleaned in an ultrasonic water bath to remove any contaminants or residues, and they were carefully inspected under an optical microscope to identify any scratches or imperfections that may have been introduced during the previous step. The final prepared samples were studied using a Zeiss Axio Observer 3 microscope at 50x magnification. Image acquisition was performed using an Infinity Lite B camera with a resolution of 1.5 megapixels, resulting in a pixel resolution of 2.5 $\mu\text{m}/\text{pixel}$. Micrographs obtained from the samples were stitched and subjected to analysis using the high-resolution misalignment analysis (HMRA) method [40], chosen for its relative insensitivity to micrographic surface quality. A cell size of 60.5 μm was selected to achieve a stable standard deviation, and a binarization threshold of 0.45 was adopted. Other important analysis parameters included setting the fiber diameter to 7 μm (as measured on the prepreg), establishing a minimum fiber diameter of 3 μm , and setting a minimum aspect ratio of 6. A 95th percentile filtering technique suggested by various authors [41, 42] was adopted to mitigate spurious measurements.

2.4 Mechanical Testing

The single-pin pullout response was assessed using a custom setup previously developed by the authors (as referenced in [29]) and schematically depicted in Fig. 3.

This setup was designed to ensure precise alignment between the loading axis of the testing machine and the samples' geometric axis. Specimens were loaded with a monotonically increasing opening displacement at a 0.5 mm/min speed up to the complete debonding into an Instron 8032 universal testing machine equipped with a 1 kN load cell. To secure the base of each sample to the testing machine's load cell, threaded connections and a spherical joint were utilized. To mitigate the effects of noise and spurious measurements induced by the compliance of the load train, pullout displacement s_c recorded by the machine was corrected with the procedure described in [29] using the formula:

$$s = s_c - \frac{F}{K^*} \quad (1)$$

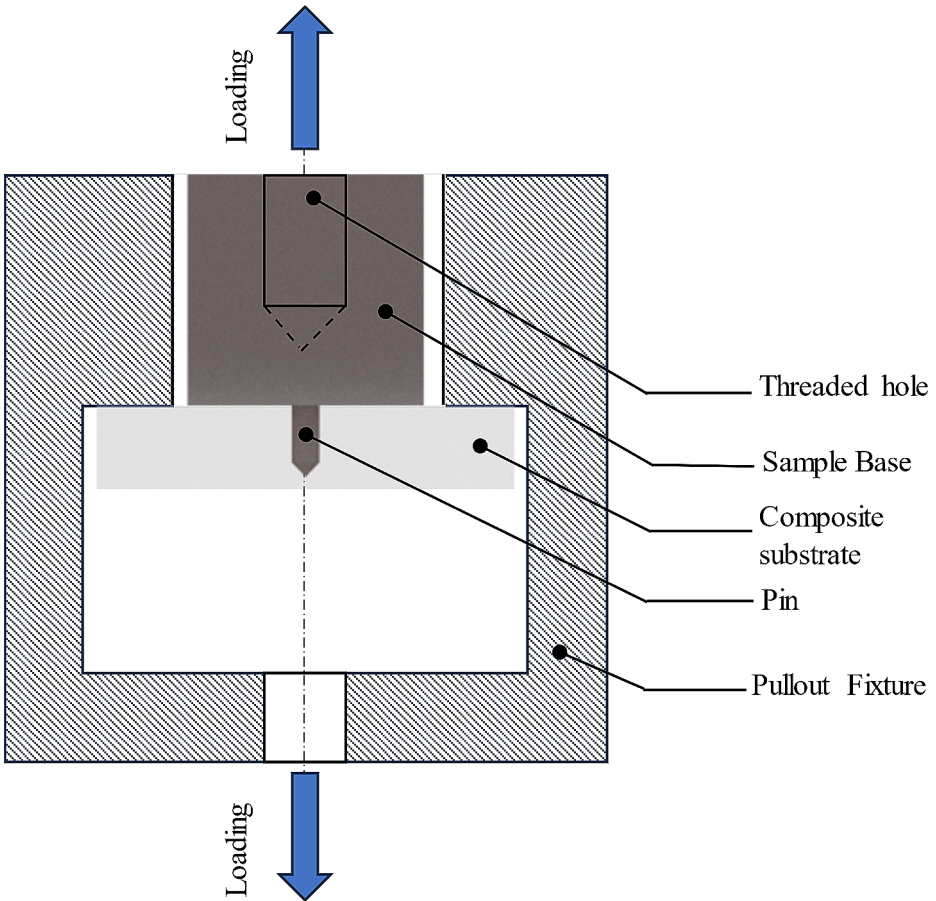


Fig. 3 Pullout test setup

where F is the opening force recorded by the load cell and K^* is the stiffness of the load train, estimated by tractioning a bulk AMPO M789 specimen in the same testing equipment.

Absorbed energy E was calculated from the pullout load F and the pullout displacements as

$$E = \int F ds \quad (2)$$

2.5 Morphological Characterization of the Fractured Surface

Following the pullout test, the fractured surfaces of the samples were initially examined using a ZEISS Stemi 508 Stereo Microscope equipped with a 5MP ZEISS Axiocam 105 color camera. This analysis aimed to investigate the macroscopic failure behavior of the

samples. The morphological fracture modes were further assessed at higher magnification through Scanning Electron Microscopy (SEM) using a Phenom ProX instrument.

3 Results and Discussion

Results from Fiber misalignment are shown and discussed in Sect. 3.1; Mechanical testing results are presented and discussed in Sect. 3.2; Results of morphological characterization of the fractured surface are shown and discussed in Sect. 3.3.

3.1 Fiber Misalignment Evaluation

Examination of various regions within Platform A through micrograph analysis uncovered multiple mechanisms affecting the microstructure of the composite substrate, corresponding to changes in the pin geometry. As visible throughout Fig. 4, the eyelet-shaped defect described in z-pin literature [27] was consistently present across all examined morphologies.

Upon inserting the 3D pin into the laminate, adjacent fibers underwent removal and lateral compression, inducing a waviness in the laminate and giving rise to a void area with an eyelike shape; subsequently, during the curing process, the void area is filled with resin, resulting in the formation of a resin-rich area where some voids can be present.

When utilizing a conventional large cylindrical pin (Fig. 4a), the internal structure of the composite substrate undergoes significant modifications due to the substantial lateral movement of the fibers to accommodate the pin. In this configuration, a pronounced swelling effect coupled with fiber dilution is present, as documented by the appearance of quite big resin pockets in the mid-planes between adjacent pins rows (Fig. 4a). On the other hand, the orientation of the fibrous material in the region surrounding the eyelike defect displays the well-documented fiber waviness, with upper values over 15° near the flanks of the resin-rich areas, as shown in Fig. 5a. When thin cylindrical pins are used to penetrate the composite substrate (Fig. 4b), the eye-shaped defect is the sole observable anomaly in the laminate, with much less misorientation defects; in fact, at a short distance from the pin, the microstructure of the fibrous material remains homogeneous and aligned in the range $[-2^\circ, 2^\circ]$ between adjacent pins rows, as demonstrated by the waviness measurements illustrated in Fig. 5b. The microstructure of the composite substrate undergoes significant changes when using arrow or double-arrow pins, as visible in Fig. 4c and d, where it can be assumed that this variation is directly attributable to the particular design of both pins. As the pin is inserted, the fibrous substrate is initially forced outwards through the pin head, which has a comparable diameter to that of a conventional pin. Afterward, the fibers may rearrange inwards around smaller diameters as insertion progresses to bridge the gap between the pin and the composite material. It can be argued that the different flow conditions of the composite material in the thickness (divergent above the pin head, convergent below the pin head) are behind the formation of the micro-cracks found in Fig. 4c and d. Misalignment analysis results for the arrow pin are presented in Fig. 5c. Outside the eye-shaped defect, in-plane waviness is consistently in the range of $[-4^\circ, 4^\circ]$ with some scatters in the proximity of microcracked regions. Similar results were obtained for the two-headed pinned sample, shown in Fig. 5d, despite some local mismatches caused by the extreme heterogeneity of the microstructure. Thin pins positioned in cequer pattern caused a slightly increased defec-

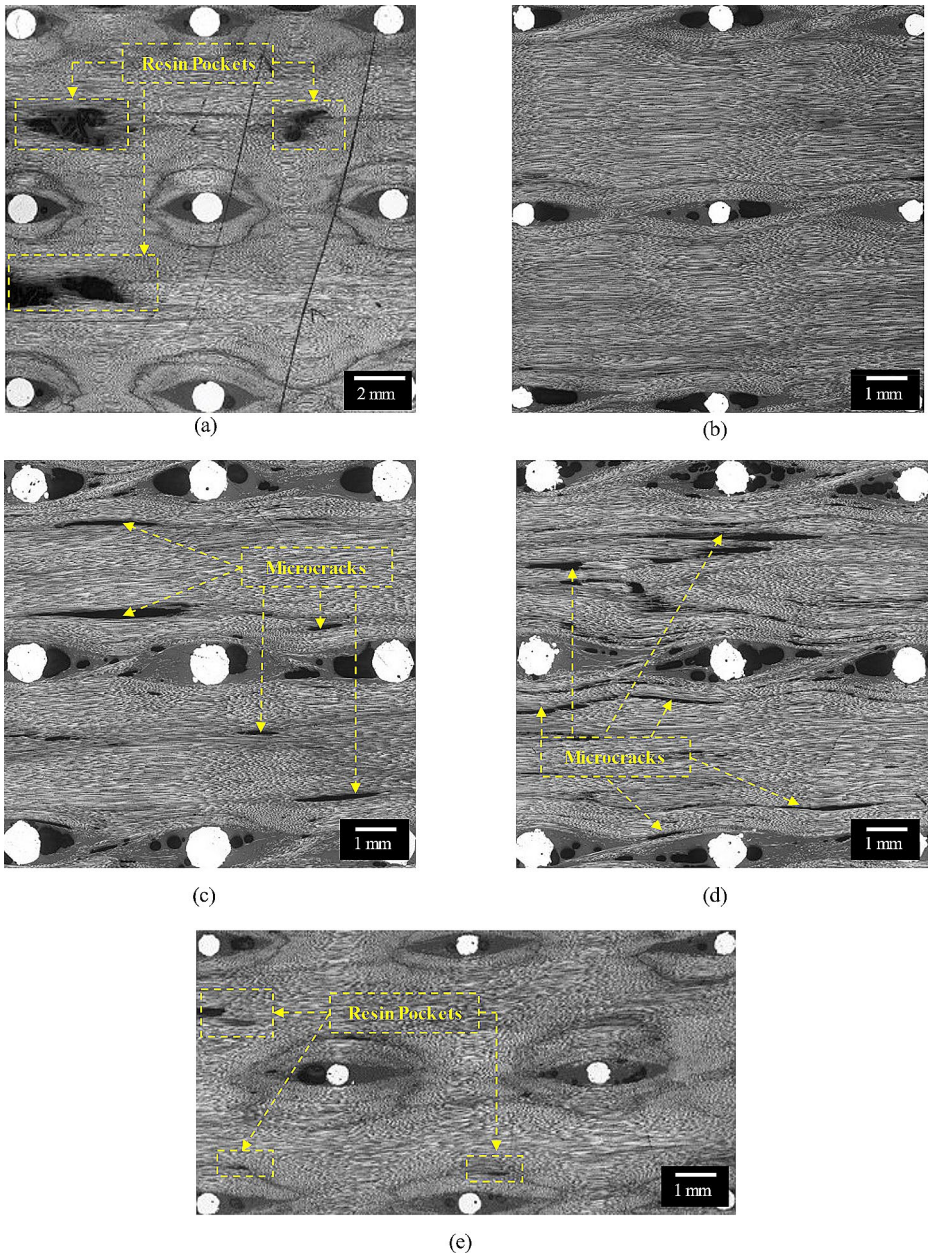


Fig. 4 Cross-sectional view of representative inner regions of Platform A, at the midplane of the arrow head: (a) conventional large cylindrical; (b) thin cylindrical; (c) arrow; (d) two-headed arrow; (e) thin cylindrical in chequer pattern

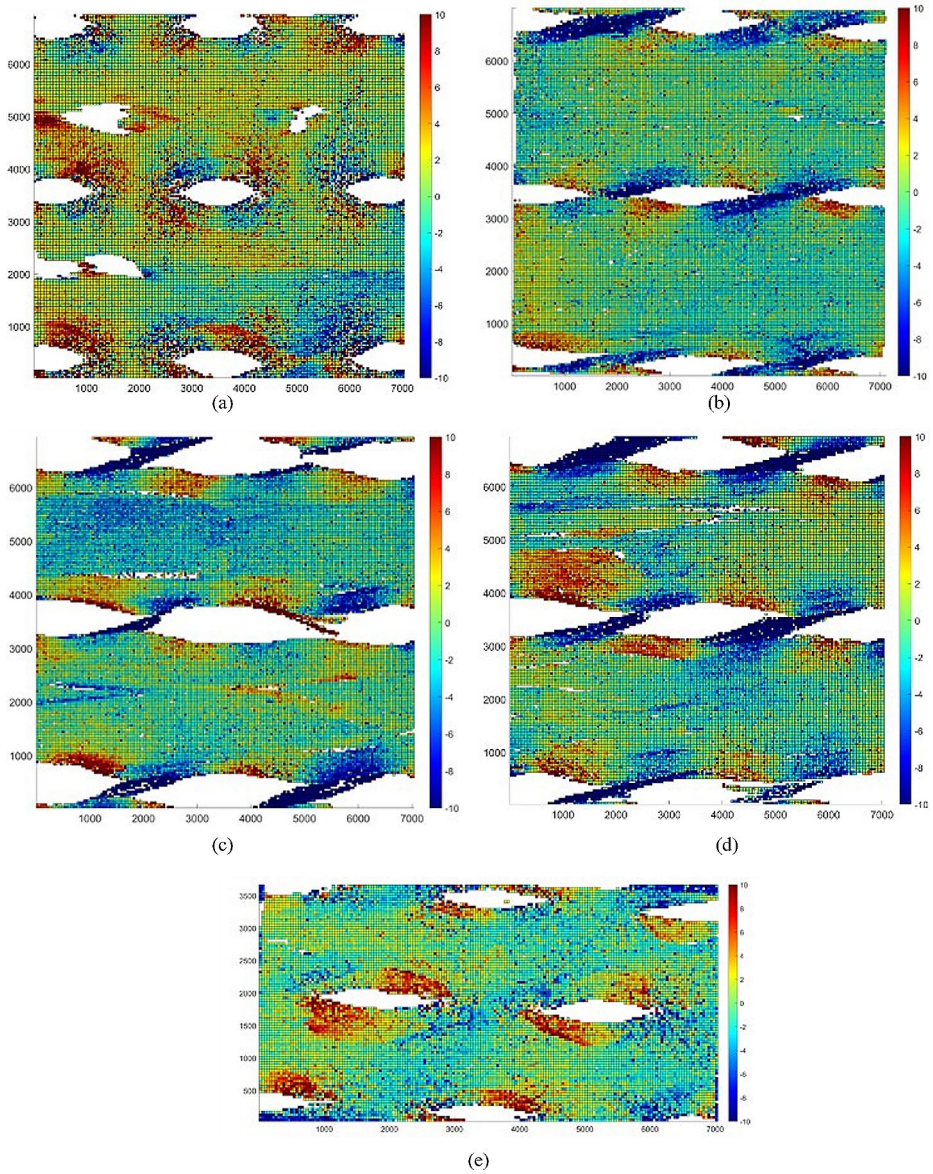


Fig. 5 Distributions of fiber misalignment angles with a spatial resolution of $60.5 \mu\text{m}$. Note that some regions exceed the minimum and maximum limits in the color bar. **(a)** conventional large cylindrical; **(b)** thin cylindrical; **(c)** arrow; **(d)** two-headed arrow

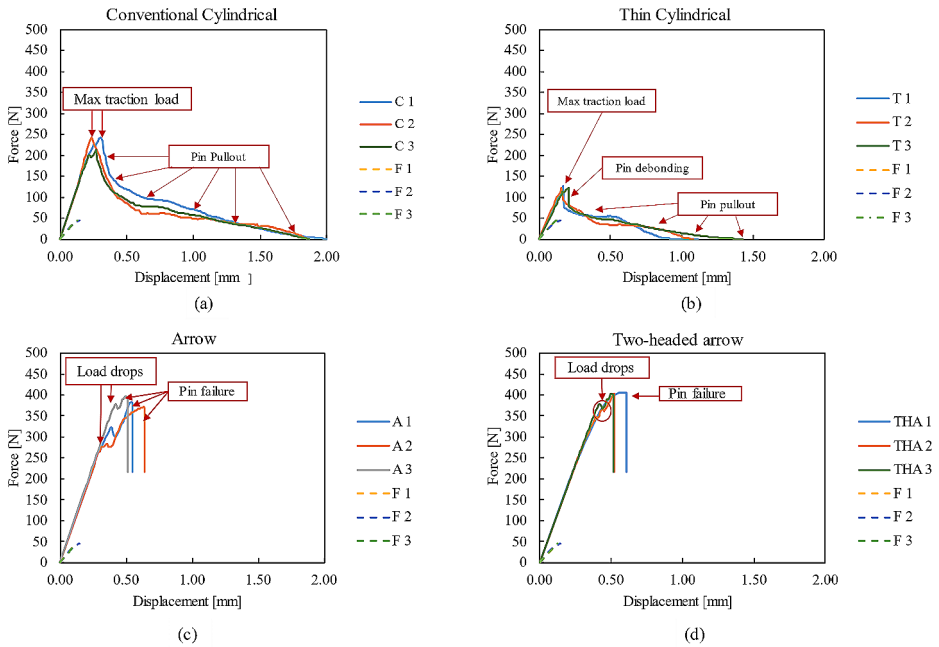


Fig. 6 Opening traction load vs. crack opening displacement curves of 3 single pin specimens for each geometry compared to flat samples (F1-F3). **(a)** conventional large cylindrical (C1-C3); **(b)** thin cylindrical (T1-T3); **(c)** arrow (A1-A3); **(d)** two-headed arrow (THA1-THA3)

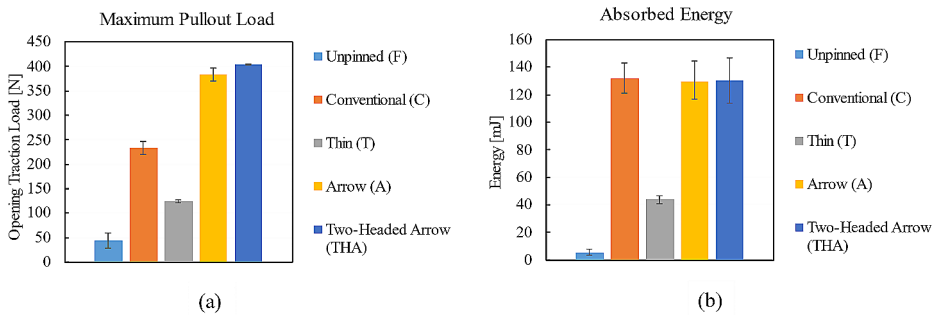


Fig. 7 Summary of experimental pullout test results of single-pin specimens with geometry features **(a)** maximum pullout load; **(b)** absorbed energy

tology in the composite substrate characterized by the presence of small resin pockets as visible in Fig. 4e. Fibrous material remains homogeneous and aligned in the range range $[-3^\circ, 3^\circ]$ between adjacent pins rows as displayed in Fig. 5e.

3.2 Mechanical Testing

Experimental pullout load-displacement results for the single-pin specimens are presented in Fig. 6 and summarized in Fig. 7. Good repeatability was seen across all configurations,

with a coefficient of variations (CV) values below 6% in maximum load and below 13% for energy absorption, except for the conventional cylindrical pin, for which a CV value of 20% was recorded. A summary of elaborated results is reported in both conventional and thin cylindrical pins, which exhibited frictional sliding pullout, while Arrow and double arrow-shaped pins led to pin fracture. The opening traction load versus crack opening displacement graphs for conventional pins demonstrated typical linear-elastic behavior until the failure of the interface, transitioning to an exponential decrease of frictional force up to the complete pull out of the pin, as shown in Fig. 6a. In thin pins, load-displacement curves exhibit an abrupt load drop after reaching the maximum, followed by the subsequent frictional pullout of the pin, as depicted in Fig. 6b.

In this configuration, the frictional force was characterized by an initial decrease followed by a significant phase of enhanced debonding/friction of the pins with high bridging forces before the final pullout phase was reached (Fig. 6b). To compare the strength of the conventional cylindrical pin and the thin one, the maximum interfacial stress τ_{max} was calculated as:

$$\tau_{max} = \frac{F_{max}}{\pi d (L - \Delta_0)} \quad (3)$$

where d and L are the diameter and length of the pin, respectively, F_{max} is the maximum opening load and Δ_0 the pin pullout displacement at F_{max} . The maximum interfacial stress was 38 MPa for the conventional cylindrical pin, with a CV (coefficient of variation) of nearly 10%, and 38 MPa for the thin pin, with a CV of 2.24%. Since the difference between the results falls within the range of experimental variability, it can be argued that the reduction in diameter does not have any impact on the strength of the interface. On the other hand, the mechanical properties of the joint are stabilized by reducing the pin diameter, as evidenced by the reduction from 10% to approximately 2% of the coefficient of variation.

Although the CVs values are calculated from only three data points in all configurations, it is still considered a reasonable indication of the variance in the results. This approach also minimizes the occurrence of microstructural defects in the composite substrate. Load-displacement curves for the Arrow and two-headed harrow pins are shown in Fig. 6c and d. All determined pullout curves exhibit a distinctive pattern characterized by elastic deformation of the pins, an intermediate load drop attributed to interface debonding, and subsequent load recovery involving plastic deformation of the pins until failure. In the case of the arrow pin, the load drops occurred at different opening tensile loads, whereas for the two-headed arrow pin, the drop happened at very much repeatable loads. Although the composite material had a more damaged microstructure, the design of the two-headed pin proved to be more effective in stabilizing the joint's mechanical properties. A substantial increase in absorbed energy is measured across all geometries with respect to the unpinned counterpart, as shown in Fig. 7b. Due to its bigger size, the conventional cylindrical pin could absorb more energy than the thin cylindrical one. On the other hand, both the Arrow and Two-headed arrow pins increased the pullout load of the joint and absorbed energies like the conventional cylindrical pin solution, thanks to metal plasticity.

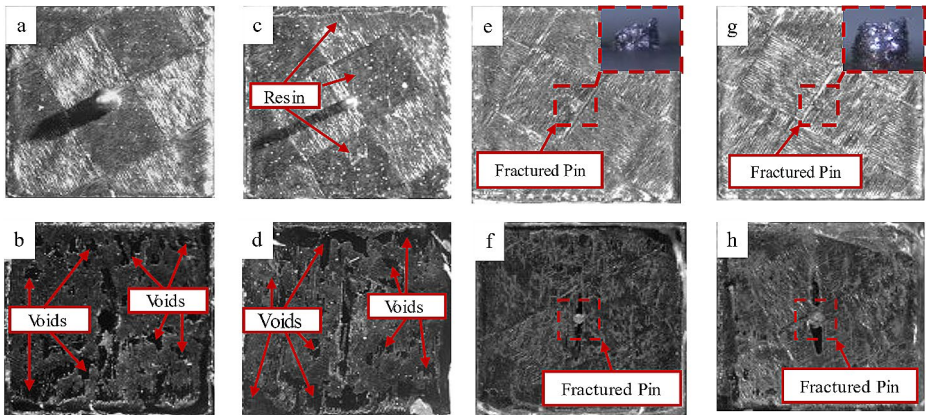


Fig. 8 Fractured surfaces of samples. (a) conventional large cylindrical pin metal substrate; (b) conventional large cylindrical pin composite substrate; (c) thin cylindrical pin metal substrate; (d) thin cylindrical pin composite substrate; (e) arrow pin metal substrate; (f) arrow pin composite substrate; (g) two-headed arrow pin metal substrate; (h) two-headed arrow pin composite substrate

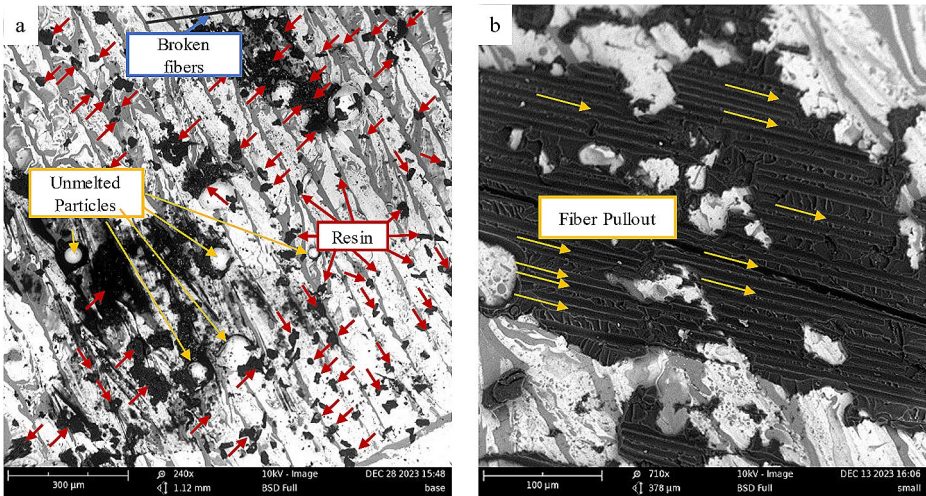


Fig. 9 Magnification of fractured areas on the metal substrate. (a) representative metal substrate with mixed adhesive/cohesive failure at a magnification of 240 \times (b) resin graft on a metallic substrate at a magnification of 710 \times

3.3 Morphological Characterization of the Fractured Surface

The analysis of the fractured specimens revealed the different failure mechanisms associated with each pin geometry, and representative results of stereomicroscopic analyses are shown in Fig. 8. The metal side of the control flat substrate showed only a minimal amount of resin residue on its base, suggesting that the samples failed due to adhesive failure. Conversely, no residual metal was detected on the CFRP side, supporting the hypothesis that the fracture was merely adhesive at the macroscale level. Regions with a limited amount of

epoxy grafts and debris were detected. With this setup, the composite substrate's interface is non-uniform, featuring alternating areas of resin richness and scarcity, as documented by the presence of the voids illustrated in Fig. 8b, which could have been caused by insufficient compaction or as a consequence of the microstructural redistribution of the composite during the insertion phase. In the cases where a thin cylindrical pin is used, the adherends' metal side displayed traces of resin in larger areas compared to conventional cylindrical pin samples. These areas are primarily located at the pin root's base, near the specimen's borders, and along the eyelike defect footprint, as illustrated in Fig. 8c. On the metal substrate of the conventional cylindrical pin (as shown in Fig. 8a), situated at the pin's root and near the borders of the specimen. This confirms that the sample experienced mixed adhesive/cohesive failure at its base, which in turn contributes to enhancing the joint's strength during pullout. Figure 8d did not reveal any metal particles on the composite substrate interface for this configuration; the resin was still unevenly distributed on the surface, with less extended void regions than those encountered on conventional cylindrical pin CFRP substrates. It can be argued that these configurations enhanced the composite material's compaction during processing thanks to the trough thickness interlocks provided by the head design of the pins.

Similar results were observed on both the Arrow and Two-headed arrow metal substrates (Fig. 8e and g). In both configurations, resin grafts and debris were consistently present close to the fractured root of the pin, along the eyelike defect footprint, and at the edges of the samples. At the same time, a marked plastic deformation of the pin at its base is consistently observable, thus confirming that a large part of the failure energy exploited during the tests by both Arrow and two-headed arrow specimens is due to the progressive yielding of those regions. The composite substrate counterparts exhibited an almost perfect distribution of the resin at the interface, as shown in Fig. 8f and h.

For all specimens, a larger magnification analysis performed on the metal substrates revealed a high number of epoxy debris in the range of 50–100 μm (Fig. 9a) as well as large areas of fractured polymeric matrix, indicating a mixed adhesive/cohesive failure at the microscale level. The finest epoxy residues were consistently found close to the valleys between adjacent hatching lines. Intermediate epoxy residues were primarily present around partially melted particles with ridges in between, produced during laser manufacturing of the samples. When the wet prepreg comes in contact with the surface, the resin flows around these particles, increasing the contact area and forming effective particle hooks within the adhesive. As observed by [23, 24] on different alloys, this interlock ultimately leads to a stronger bond between AMPO M789 and epoxy, outperforming pure adhesive strength alone without requiring additional surface treatment methods [43]. More significant resin grafts with pulled-out fibers (Fig. 9b) were found in proximity to the pin roots and along the edges and Representative fracture surfaces of the different pin geometries are shown in Fig. 10. Without exception, all of the hybrid joints initially failed due to the growth of cracks along the interface between the substrates. Along pin length, two different textured surface regions were identified in conventional and thin cylindrical pins: a coarse-textured surface region and a smoother-textured surface region, as shown in Fig. 10a and b. The surface close to the base of the pin was consistently found to be coarse-textured; this area contained partially melted metal particles that could firmly adhere to the epoxy resin.

As visible in Fig. 10a and b, fibers were found embedded into the adhesive matrix in this region, confirming that the prepreg could reach the pin root for both configurations. Along the pullout direction, the pin surface displayed varying morphologies, with some regions

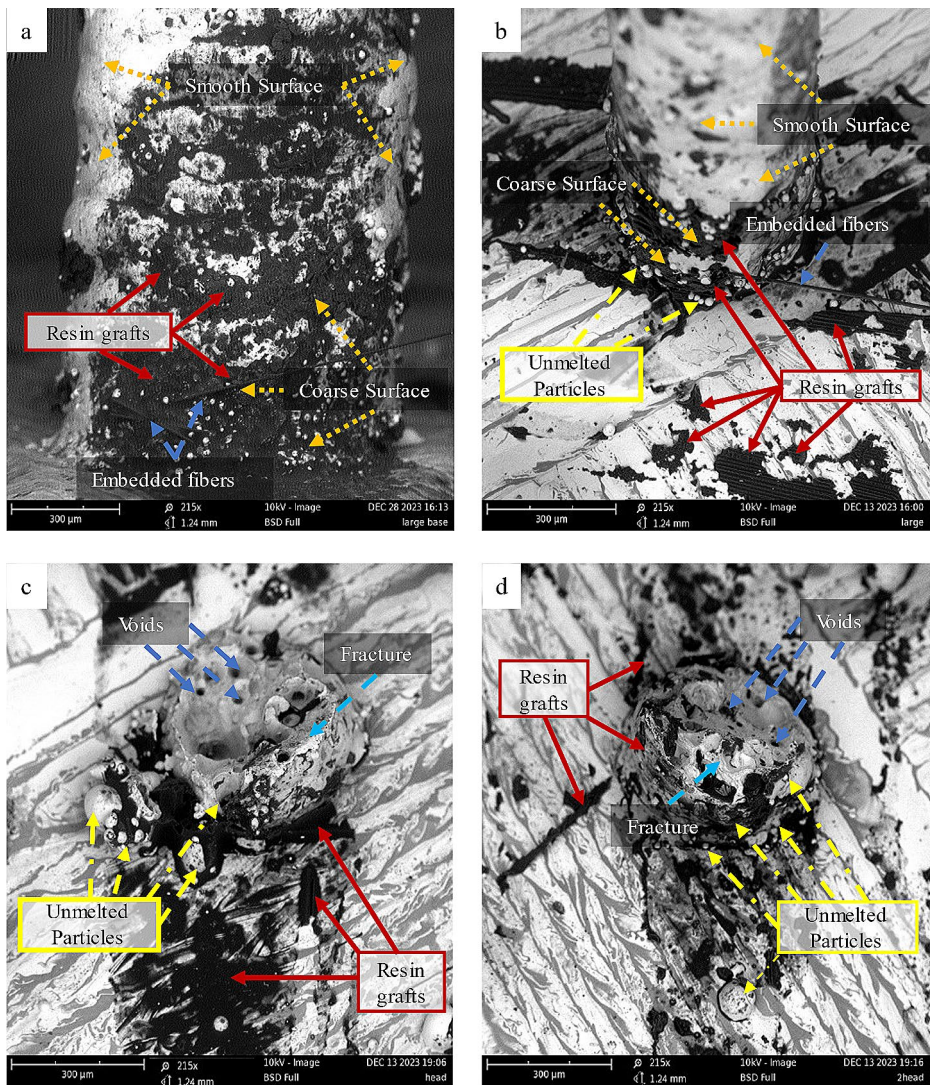


Fig. 10 Scanning electron micrographs showing fracture surfaces of different pin shapes onto the metal substrate. (a) conventional large cylindrical; (a) thin cylindrical; (c) arrow; (d) two-headed arrow

being coarse-textured and others being smoother-textured. The smoother regions had minimal resin residues and fewer partially melted particles, indicating that they experienced significant abrasion during mechanical testing. Figure 10a shows a more gradual transition between the coarse and smooth textured surface for the conventional cylindrical pin compared to the thin pin sample shown in Fig. 10b, further justifying the different trends in pullout exhibited by the two geometries (see Sect. 3.2). Both fractured Arrow (Fig. 10c) and Two-headed Arrow (Fig. 10e) pins exhibited a coarse-textured surface at their bases, similar to the thin cylindrical pin. Resin graft and resin-embedded unmelted particles were consistently present. corners shared with neighboring squares of the chessboard pattern adopted to

manufacture the metallic adherend. Voids in the cup-cones fractured areas suggest a moderate ductile failure of both pins geometries.

4 Conclusions

Pin size and shape can be effectively used to fine tune the behavior of a hybrid material metal-composite joint with respect to the conventional 1 mm pin cylindrical solution present in literature. In this work, the following was found:

- Both thin and conventional design lead to a pullout mechanism lead by slipping. Thinner cylindrical pins of 0.5 mm in diameter determine much more minor damage in the composite structure while keeping the maximum tensile stress at the interface of the conventional 1 mm diameter one. This can lead to better design of cylindrical pins hybrid joints where the same global pin interface is generated by more pins of smaller size.
- Using simple-arrow or two-headed arrow pins instead of cylindrical ones can significantly increase interfacial pullout strength by forcing the pin fracture to be the primary failure mechanism. This can be achieved while maintaining the same pullout energy level and fiber defects as the conventional 1 mm cylindrical solution. In particular, the two-headed arrow pins configuration effectively improves the mechanical behavior of the joint and the consistency of the results.

This study focuses on reinforcement effect of different metal anchors based on single pin specimens. Future works will analyze numerically the multimaterial joint formation by means of virtual process simulations. Structural finite element analysis will be performed to understand the impact of main geometric parameters over failure mechanism of the joint such as base debonding, pin debonding, pin fracture or composite failure. This will allow for an optimal pin design were both composite sliding and pin fracturing occurs, to fully exploit the strength potential of each material constituent. Different loading condition will be tested to provide a more extensive understanding on the toughening potential of micro penetrative anchoring technique. Scalability of the technique on large assemblies with multiple reinforcement pins at different densities will be demonstrated.

Author Contributions LR: Conceptualization, Formal analysis, Investigation, Methodology, Supervision, Visualization, Writing – original draft. LT: Conceptualization, Formal analysis, Investigation, Methodology, Visualization, Writing – original draft. AZ: Conceptualization, Formal analysis, Investigation, Methodology, Writing – review & editing.

Funding Project funded under the National Recovery and Resilience Plan (NRRP), Mission 04 Component 2 Investment 1.5—NextGenerationEU, Call for tender n. 3277 dated 30 December 2021 Award Number: 0001052 dated 23 June 2022 CUP: B33D21019790006.

Funding Open access funding provided by Alma Mater Studiorum - Università di Bologna within the CRUI-CARE Agreement.

Data Availability The raw/processed data required to reproduce these findings cannot be shared at this time as the data also forms part of an ongoing study.

Declarations

Competing Interest The authors declare that they have no known competing financial interests or personal relationships that could have appeared to influence the work reported in this paper.

Open Access This article is licensed under a Creative Commons Attribution 4.0 International License, which permits use, sharing, adaptation, distribution and reproduction in any medium or format, as long as you give appropriate credit to the original author(s) and the source, provide a link to the Creative Commons licence, and indicate if changes were made. The images or other third party material in this article are included in the article's Creative Commons licence, unless indicated otherwise in a credit line to the material. If material is not included in the article's Creative Commons licence and your intended use is not permitted by statutory regulation or exceeds the permitted use, you will need to obtain permission directly from the copyright holder. To view a copy of this licence, visit <http://creativecommons.org/licenses/by/4.0/>.

References

- Mouritz, A.P.: Introduction to Aerospace Materials. (2012). <https://doi.org/10.2514/4.869198>
- Staff, G.G.: Is the BMW 7 Series the future of autocomposites? *CompositesWorld* 2016
- Díaz-Álvarez, A., Rodríguez-Millán, M., Díaz-Álvarez, J., Miguélez, M.H.: Experimental analysis of drilling induced damage in aramid composites. *Compos. Struct.* **202**, 1136–1144 (2018). <https://doi.org/10.1016/j.compstruct.2018.05.068>
- Li, W., Frederick, H., Palardy, G.: Multifunctional films for thermoplastic composite joints: Ultrasonic welding and damage detection under tension loading. *Compos. Part. Appl. Sci. Manuf.* **141**, 106221 (2021). <https://doi.org/10.1016/j.compositesa.2020.106221>
- Li, W., Palardy, G.: Investigation of welding repair methods for thermoplastic composite joints. *Compos. Part. B Eng.* **264**, 110924 (2023). <https://doi.org/10.1016/j.compositesb.2023.110924>
- Martinsen, K., Hu, S.J., Carlson, B.E.: Joining of dissimilar materials. *CIRP Ann. - Manuf. Technol.* **64**, 679–699 (2015). <https://doi.org/10.1016/j.cirp.2015.05.006>
- Zhuang, W., Chen, S., Liu, Y.: Influence of joining temperature on damage of warm self-piercing riveted joints in carbon fiber reinforced polymer and aluminum alloy sheets. *J. Manuf. Process.* **89**, 77–91 (2023). <https://doi.org/10.1016/j.jmapro.2023.01.062>
- Zeinedini, A., Hosseini, Y., Mahdi, A.S., Akhavan-Safar, A., da Silva, L.F.M.: Impact of the Manufacturing process on the Flexural properties of laminated Composite-Metal riveted joints: Experimental and Numerical studies. *Appl. Compos. Mater.* (2023). <https://doi.org/10.1007/s10443-023-10186-w>
- von Silva, H.P.F., Camanho, M.T., Marques, P.P., Castro, A.T.: 3D-reinforcement techniques for co-bonded CFRP/CFRP and CFRP/metal joints: A brief review. *Cienc. e Tecnol Dos Mater.* **29**, e102–e107 (2017). <https://doi.org/10.1016/j.ctmat.2016.07.011>
- Sarantinos, N., Tsantzalis, S., Ucsnik, S., Kostopoulos, V.: Review of through-the-thickness reinforced composites in joints. *Compos. Struct.* **229** (2019). <https://doi.org/10.1016/j.compstruct.2019.111404>
- Wang, X., Ahn, J., Bai, Q., Lu, W., Lin, J.: Effect of forming parameters on electron beam Surf-I-Sculpt protrusion for Ti-6Al-4V. *Mater. Des.* **76**, 202–206 (2015). <https://doi.org/10.1016/j.matdes.2015.03.065>
- Skhabovskiy, I., Batista, N.L., Damato, C.A., Reis, R.P., Botelho, E.C., Scotti, A.: Appraisal of fiber-metal laminate panels reinforced with metal pins deposited by CMT welding. *Compos. Struct.* **180**, 263–275 (2017). <https://doi.org/10.1016/j.compstruct.2017.07.043>
- Ucsnik, S., Stelzer, S., Sehrschön, H., Sieglhuber, G.: Composite to composite joint with lightweight metal reinforcement for enhanced damage tolerance. 16th Eur. Conf. Compos. Mater. ECCM. 2014. (2014)
- Heimbs, S., Nogueira, A.C., Hombergsmeier, E., May, M., Wolfrum, J.: Failure behaviour of composite T-joints with novel metallic arrow-pin reinforcement. *Compos. Struct.* **110**, 16–28 (2014). <https://doi.org/10.1016/j.compstruct.2013.11.022>
- Bagnato, T., Ravindran, A.R., Mirabedini, A., Ladani, R.B., Kandare, E., Orifici, A.C., et al.: Superior interfacial toughening of hybrid metal-composite structural joints using 3D printed pins. *Compos. Part. Appl. Sci. Manuf.* **168** (2023). <https://doi.org/10.1016/j.compositesa.2023.107479>
- Jasiūnienė, E., Mažeika, L., Samaitis, V., Cicėnas, V., Mattsson, D.: Ultrasonic non-destructive testing of complex titanium/carbon fibre composite joints. *Ultrasonics.* **95**, 13–21 (2019). <https://doi.org/10.1016/j.ultras.2019.02.009>

17. De Pasquale, G., Coluccia, A.: Modeling and experimental validation of CFRP-Metal joints utilizing 3D additively manufactured anchors. *J. Manuf. Sci. Eng.* **145**, 1–13 (2023). <https://doi.org/10.1115/1.4063110>
18. Yap, C.Y., Chua, C.K., Dong, Z.L., Liu, Z.H., Zhang, D.Q., Loh, L.E., et al.: Review of selective laser melting: Materials and applications. *Appl. Phys. Rev.* **2** (2015). <https://doi.org/10.1063/1.4935926>
19. DebRoy, T., Wei, H.L., Zuback, J.S., Mukherjee, T., Elmer, J.W., Milewski, J.O., et al.: Additive manufacturing of metallic components – process, structure and properties. *Prog Mater. Sci.* **92**, 112–224 (2018). <https://doi.org/10.1016/j.pmatsci.2017.10.001>
20. Parkes, P.N., Butler, R., Meyer, J., de Oliveira, A.: Static strength of metal-composite joints with penetrative reinforcement. *Compos. Struct.* **118**, 250–256 (2014). <https://doi.org/10.1016/j.compstruct.2014.07.019>
21. Zhang, Y., Liu, T., Ren, H., Maskery, I., Ashcroft, I.: Dynamic compressive response of additively manufactured AlSi10Mg alloy hierarchical honeycomb structures. *Compos. Struct.* **195**, 45–59 (2018). <https://doi.org/10.1016/j.compstruct.2018.04.021>
22. Arjunan, A., Singh, M., Baroutaji, A., Wang, C.: Additively manufactured AlSi10Mg inherently stable thin and thick-walled lattice with negative Poisson's ratio. *Compos. Struct.* **247** (2020). <https://doi.org/10.1016/j.compstruct.2020.112469>
23. Nguyen, A.T.T., Brandt, M., Orifici, A.C., Feih, S.: Hierarchical surface features for improved bonding and fracture toughness of metal-metal and metal-composite bonded joints. *Int. J. Adhes. Adhes.* (2016). <https://doi.org/10.1016/j.ijadhadh.2015.12.005>
24. Raimondi, L., Tomesani, L., Donati, L., Zucchelli, A.: Lattice material infiltration for hybrid metal-composite joints: Manufacturing and static strength. *Compos. Struct.* **269**, 114069 (2021). <https://doi.org/10.1016/j.compstruct.2021.114069>
25. Nguyen, A.T.T., Amarasinghe, C.K., Brandt, M., Feih, S., Orifici, A.C.: Loading, support and geometry effects for pin-reinforced hybrid metal-composite joints. *Compos. Part. Appl. Sci. Manuf.* **98**, 192–206 (2017). <https://doi.org/10.1016/j.compositesa.2017.03.019>
26. Kostopoulos, V., Sarantinos, N., Tsantalis, S.: Review of through-the-thickness reinforced z-pinned composites. *J. Compos. Sci.* **4** (2020). <https://doi.org/10.3390/jcs4010031>
27. Mouritz, A.P.: Review of z-pinned composite laminates. *Compos. Part. Appl. Sci. Manuf.* **38**, 2383–2397 (2007). <https://doi.org/10.1016/j.compositesa.2007.08.016>
28. Eberl, L., Avila Gray, L., Zarella, S., Drechsler, K.: The effect of fiber undulation on the strain field for pinned composite/titanium joints under tension. *Compos. Part. Appl. Sci. Manuf.* **103**, 148–160 (2017). <https://doi.org/10.1016/j.compositesa.2017.09.015>
29. Tang, S., Lemanski, S., Zhang, X., Ayre, D.: Fatigue life prediction of z-fibre pinned composite laminate under mode I loading. *Compos. Sci. Technol.* **174**, 221–231 (2019). <https://doi.org/10.1016/j.compscitech.2019.02.010>
30. Wang, X.X., Chen, L., Jiao, Y.N., Li, J.L.: Preparation of carbon fiber powder-coated Z-pins and experimental study on the mode I delamination toughening properties. *Polym. Compos.* **37**, 3508–3515 (2016). <https://doi.org/10.1002/pc.23550>
31. Li, M., Chen, P.: A numerical study of the influence of Z-pin parameters on the elastic properties of laminates. *Polym. Polym. Compos.* **29**, 1390–1402 (2021). <https://doi.org/10.1177/0967391120970086>
32. Cheng, L., Ji, G., Fei, S., Li, J., Ke, Y.: Investigation on insertion mechanism of ultrasound guided insertion process based on numerical simulation. *Polym. Compos.* **43**, 7303–7314 (2022). <https://doi.org/10.1002/pc.26796>
33. Nguyen, A.T.T., Pichitdej, N., Brandt, M., Feih, S., Orifici, A.C.: Failure modelling and characterization for pin-reinforced metal-composite joints. *Compos. Struct.* **188**, 185–196 (2018). <https://doi.org/10.1016/j.compstruct.2017.12.043>
34. Mouritz, A.P., Koh, T.M.: Re-evaluation of mode I bridging traction modelling for z-pinned laminates based on experimental analysis. *Compos. Part. B Eng.* **56**, 797–807 (2014). <https://doi.org/10.1016/j.compositesb.2013.09.016>
35. Cui, P., Xing, G., Nong, Z., Chen, L., Lai, Z., Liu, Y., et al.: Recent advances on Composition-Microstructure-Properties Relationships of Precipitation Hardening Stainless Steel. *Mater. (Basel)*. **15** (2022). <https://doi.org/10.3390/ma15238443>
36. Morri, A., Zanni, M., Ceschini, L., Fortunato, A., Pellizzari, M.: Aging Behaviour of a 12.2Cr-10Ni-1Mo-1Ti-0.6Al Precipitation-Hardening Stainless Steel Manufactured via Laser Powder Bed Fusion. *Met. (Basel)*. **13**, 1552 (2023). <https://doi.org/10.3390/met13091552>
37. Popp, J., Kleffel, T., Römisch, D., Papke, T., Merklein, M., Drummer, D.: Fiber orientation mechanism of continuous Fiber Reinforced Thermoplastics Hybrid Parts joined with metallic pins. *Appl. Compos. Mater.* **28**, 951–972 (2021). <https://doi.org/10.1007/s10443-021-09892-0>

38. Nguyen, A.T.T., Brandt, M., Feih, S., Orifici, A.C.: Pin pull-out behaviour for hybrid metal-composite joints with integrated reinforcements. *Compos. Struct.* **155**, 160–172 (2016). <https://doi.org/10.1016/j.compstruct.2016.07.047>
39. Stewart, A.L., Poursartip, A.: Characterization of fibre alignment in as-received aerospace grade unidirectional prepreg. *Compos. Part. Appl. Sci. Manuf.* (2018). <https://doi.org/10.1016/j.compositesa.2018.04.018>
40. Wilhelmsson, D., Asp, L.E.: A high resolution method for characterisation of fibre misalignment angles in composites. *Compos. Sci. Technol.* (2018). <https://doi.org/10.1016/j.compscitech.2018.07.002>
41. Wilhelmsson, D., Gutkin, R., Edgren, F., Asp, L.E.: An experimental study of fibre waviness and its effects on compressive properties of unidirectional NCF composites. *Compos Part A Appl Sci Manuf* 2018. <https://doi.org/10.1016/j.compositesa.2018.02.013>
42. Raimondi, L., Brugo, T.M., Zucchelli, A.: Fiber misalignment analysis in PCM-UD composite materials by full field nodal method. *Compos. Part. C Open. Access.* **5** (2021). <https://doi.org/10.1016/j.jcomc.2021.100151>
43. Gulino, M., Moroni, F., Pirondi, A.: Metal-metal and metal-composite joints with 3D printed aluminium substrates: Effect of surface treatment on the mode I fracture toughness. *J. Adhes.* **00**, 1–29 (2023). <https://doi.org/10.1080/00218464.2023.2285074>

Publisher's Note Springer Nature remains neutral with regard to jurisdictional claims in published maps and institutional affiliations.